Materials and Design 86 (2015) 545–554

Contents lists available at ScienceDirect

Materials and Design

journal homepage: www.elsevier.com/locate/jmad

Influence of defects on mechanical properties of Ti–6Al–4 V components produced by selective laser melting and electron beam melting

Haijun Gong [a], Khalid Rafi [b], Hengfeng Gu [c], G.D. Janaki Ram [d], Thomas Starr [a], Brent Stucker [e,*]

[a] J. B. Speed School of Engineering, University of Louisville, Louisville, KY, United States
[b] UL International-Singapore Pte Ltd, Singapore
[c] College of Engineering, North Carolina State University, Raleigh, NC, United States
[d] Dept. of Metallurgical and Materials Engineering, IIT Madras, Chennai 600 036, India
[e] 3DSIM LLC, Park City, UT, United States

ARTICLE INFO

Article history:
Received 20 March 2015
Received in revised form 2 July 2015
Accepted 27 July 2015
Available online 30 July 2015

Keywords:
Additive manufacturing
Selective laser melting
Electron beam melting
Ti–6Al–4 V
Defects
Mechanical properties

ABSTRACT

This study evaluates the mechanical properties of Ti–6Al–4 V samples produced by selective laser melting (SLM) and electron beam melting (EBM). Different combinations of process parameters with varying energy density levels were utilized to produce samples, which were analyzed for defects and subjected to hardness, tensile, and fatigue tests. In SLM samples, small pores in amounts up to 1 vol.% resulting from an increase in energy density beyond the optimum level were found to have no major detrimental effect on the mechanical properties. However, further increase in the energy density increased the amount of porosity to 5 vol.%, leading to considerable drop in tensile properties. Samples produced using lower-than-optimum energy density exhibited unmelted powder defects, which, even at 1 vol.% level, strongly affected both tensile and fatigue properties. In EBM, insufficient energy input was found to result in large, macroscopic voids, causing serious degradation in all mechanical properties. These findings are helpful in process optimization and standardization of SLM and EBM processes.

1. Introduction

Additive manufacturing (AM) produces parts directly from three-dimensional CAD data, layer upon layer. Selective laser melting (SLM) and electron beam melting (EBM) are two commonly used AM processes based on powder bed fusion. In SLM, a metallic powder is spread into a thin layer and a finely focused laser selectively melts the powder, fusing it to the previous layer [1]. Part fabrication takes place inside a chamber filled with inert gas. Many different metal powders can be utilized for part fabrication in SLM, including stainless steel, maraging steel, cobalt–chromium and titanium alloys [2–4]. The EBM process is similar to the SLM process, but makes use of an electron beam for selectively melting the metal powder. In contrast to SLM, part fabrication in EBM takes place inside a vacuum chamber and the powder surrounding the part is maintained at an elevated temperature. At present, EBM is mainly used for producing parts in titanium alloys [1,5,6].

Because of their layered microstructure, the mechanical behavior of AM parts can be significantly different from conventionally manufactured parts. Further, AM parts can develop a variety of defects due to improper choice of process parameters or process disturbances. For example, incomplete wetting and balling effects associated with insufficient energy input lead to pores or voids in SLM parts [7,8]. Similarly, when the energy input is not sufficient, successive scan tracks do not properly fuse together and defects appear along the scan lines [4,9]. EBM parts generally show large voids or cavities extending across several layers when the process parameters are not carefully chosen. Smaller spherical pores can also develop in EBM parts due to entrapment of gases originally present in gas-atomized metal powders [10]. While these defects can be expected to be detrimental to part mechanical properties, how different types of defects influence the mechanical properties and what type of defects can be tolerated in what amounts in AM parts is a matter of current interest and study.

A number of studies are available on the mechanical properties (mainly, hardness, tensile, and fatigue) of SLM and EBM Ti–6Al–4 V parts [11–14]. In general, porosity was found to have a strong impact on the mechanical properties of SLM and EBM parts, especially dynamic properties [15,16]. Santos et al. [17] conducted laser melting of pure titanium powder and fabricated specimens with densities higher than 95%. While these samples showed comparable tensile strength to wrought material, their impact and torsional fatigue strengths were rather low because of porosity. Gong et al. [18], Edwards et al. [19], Wycisk et al. [20], and Simonelli et al. [21] also reported inferior uniaxial fatigue performance in Ti–6Al–4 V SLM parts due to porosity. Leuders et al. [22] suggested that micron-sized pores mainly affect fatigue strength, while residual stresses have a strong bearing on the fatigue crack growth. Li et al. [23] carried out compression fatigue tests on Ti–6Al–4 V mesh arrays (these can be regarded as parts containing

* Corresponding author at: 3DSIM LLC, Park City, UT 84098, United States.
E-mail address: brent.stucker@3dsim.com (B. Stucker).

http://dx.doi.org/10.1016/j.matdes.2015.07.147
0264-1275/

Table 1
Process parameters used for SLM.

Parameter set	Scan speed (mm/s)	Energy density (J/mm^3)
SLM-OP 1	960	42
SLM-MP 2	540	74
SLM-MP 3	400	100
SLM-MP 4	1260	32
SLM-MP 5	1500	27

Note: Laser power (120 W), hatch spacing (0.1 mm), layer thickness (0.03 mm) were the same in all the cases.

Table 2
Process parameters used for EBM (the layer thickness was 0.05 mm in all the cases).

Parameter no.	Max current (mA)	Speed function index	Line offset (mm)	Focus offset (mA)
EBM-OP 1	21	98	0.1	3
EBM-MP 2	30	60	0.2	15
EBM-MP 3	20	180	0.2	5

deterministic defects) with very high porosity levels (60–85 vol.%). It was found that the fatigue strength increased with increasing relative density. Brenne et al. [24] conducted four-point-bend tests and fatigue tests on Ti–6Al–4 V cellular structures produced using SLM in as-built and heat treated (1050 °C/2 h/furnace cooling) conditions. Digital image correlation (DIC) techniques were utilized to investigate the local strains. Considerable improvements in bend and fatigue performance were reported after the heat treatment. Sun et al. [25] and Amin Yavari et al. [26] studied the effect of unit cell structure on the mechanical properties of Ti–6Al–4 V cellular parts. They have shown that the geometrical morphology of the defect or the porous structure can strongly influence the mechanical strength. Vandenbroucke et al. [4] investigated the hardness of SLM-built Ti–6Al–4 V samples and showed that porosity can affect macro hardness, but not micro hardness. Heinl et al. [27] evaluated the compressive strength of non-stochastic cellular Ti–6Al–4 V structure fabricated by EBM. Murr et al. [28,29] also studied EBM Ti–6Al–4 V cellular structures and stochastic foams. It has been shown that the stiffness of these structures having designed porosity varies with density, and varies inversely with porosity. Schwerdtfeger et al. [30,31] and Li et al. [32] investigated non-stochastic cellular auxetic structures (i.e., deterministic defects) built from Ti–6Al–4 V using EBM. They observed a good correlation between Young's modulus and Poisson's ratio, and relative density and internal structure. Similarly, Yang et al. [33] investigated the compressive properties of Ti–6Al–4 V auxetic mesh structures produced by EBM. They showed that re-entrant lattice structures possess superior mechanical properties compared to regular foam structures.

Many researchers have reported how process parameters influence defect generation in SLM and EBM [34–38]. In this work, we report the mechanical properties of SLM and EBM Ti–6Al–4 V samples containing various types and amounts of defects. Broadly, two types of defects are dealt with: (i) defects due to incomplete powder melting or improper fusion between successive tracks or layers, (ii) defects due to entrapment of gases or improper closure of a keyhole. Defects of the former type arise due to insufficient energy input, while the latter are caused by the use of excessive energy.

2. Experimental details

Ti–6Al–4 V powder (Grade 23) obtained from Advanced Powders and Coatings Inc., Canada, was used for SLM. The powder has an apparent density of 2.6 g/cm^3 and a mean particle size of ~ 30 μm (D_{10}: 17 μm, D_{90}: 44 μm). For EBM, Ti–6Al–4 V powder (Grade 23) supplied by Arcam was used. This powder has an apparent density of 2.7 g/cm^3 with a mean particle size of 73 μm (D_{10}: 47 μm, D_{90}:99 μm). Both the powders are spherical. Note that the powder used in EBM is considerably coarser than that used in SLM.

SLM and EBM experiments were conducted using EOS M270 DMLS and Arcam S400 machines, respectively. Cylindrical bars (10 mm in diameter) were built in the *Z* orientation (ISO/ASTM 52921, 2013) using different combinations of process parameters, as shown in Table 1 (for SLM) and Table 2 (for EBM). In SLM, the energy density was varied at two levels above (parameter sets SLM-MP2 and SLM-MP3) and below

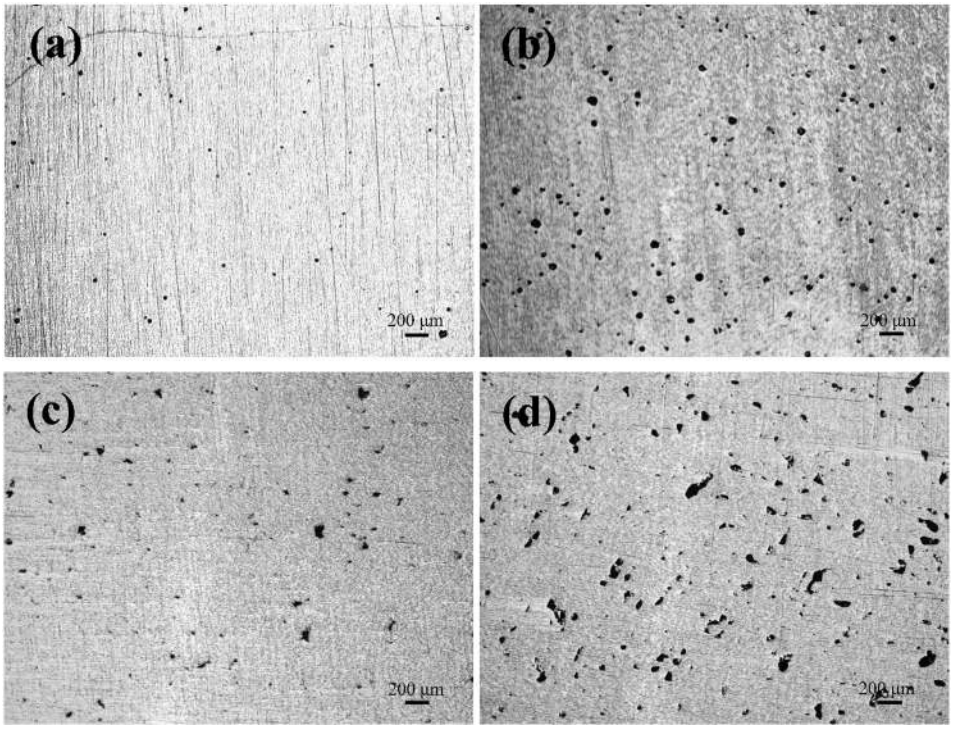

Fig. 1. Optical micrographs of SLM samples in as-polished condition: (a) SLM-MP2, (b) SLM-MP3, (c) SLM-MP4, (d) SLM-MP5.

Table 3
Results of bulk density measurements by the Archimedes method.

Parameter set	Density (g/cm^3)	Estimated porosity (vol.%)
SLM		
SLM-OP 1	4.41	0
SLM-MP 2	4.37	1
SLM-MP 3	4.21	5
SLM-MP 4	4.37	1
SLM-MP 5	4.20	5
EBM		
EBM-OP 1	4.41	0
EBM-MP 2	4.38	1
EBM-MP 3	4.22	5

Note: For porosity estimation, the nominal density of Ti–6Al–4 V was taken as 4.41 g/cm^3. SLM-OP1 and EBM-OP1 samples contained some sparse pores, which, however, did not affect their density.

(parameter sets SLM-MP4 and SLM-MP5) the optimum energy density (parameter set SLM-OP1). This was done by changing the scan speed (V), which is related to energy density (E), as below:

$$E = \frac{P}{V * h * t}$$

where P is laser power, h is hatch spacing, and t is layer thickness. The optimum process parameters were determined in a previous study [35].

In the case of EBM, as detailed in Table 2, certain deviations (parameter sets EBM-MP2 and EBM-MP3) from the recommended machine/parameter settings for Ti–6Al–4 V (parameter set EBM-OP1) were attempted. These parametric variations were chosen based on a previous study on the effects of process parameters on defect generation in EBM [35]. Note that the parameters listed in Table 2 were the actual machine settings and/or control algorithms used for making the samples. Specific values of beam current (the maximum value can be specified) and scan speed are continuously varied throughout the build according to the speed function setting. Line offset determines the distance between successive scan lines and focus offset determines the beam diameter (a higher focus offset results in a higher beam diameter).

No heat treatment was performed on any of the samples produced in the current study. Metallographic specimens were prepared using standard grinding and polishing procedures, and etched by Kroll's reagent (92 ml H_2O, 5 ml HNO_3, and 3 ml HF). An Olympus MX51 optical microscope was used for microstructural examination. The density of the samples made using different process parameters was measured using the Archimedes method as per ASTM B962-08. All the samples were lightly sand blasted and polished before density measurements. Hardness testing was done on a Rockwell C-Scale tester employing a diamond cone (Brale) indenter as per ASTM E18. Standard tensile and fatigue test specimens were machined from the samples built using various process parameters. Tensile tests were carried out as per ASTM E8 on an Instron 5569A tensile testing machine with Bluehill® 2 testing software using a crosshead travel speed of 2.5 mm/min. Tests were carried out using a static axial clip-on extensometer attached to the gage section of the specimen. For each process parameter set, six samples were tested. High cycle fatigue tests were performed as per ASTM E466 on a 10 kN Instron Electropulse 10000 fatigue testing machine with WaveMatrix™ testing software. Fatigue tests were conducted using sinusoidal loading (maximum stress = up to 750 MPa, stress ratio $R = 0.1$) at a frequency of 50 Hz. More than ten specimens were tested for each process parameter combination at different maximum stress levels. Fatigue testing was discontinued after 10^7 cycles. All the tests were conducted at room temperature. After the tests, fracture surfaces were examined using a FEI Nova NanoSEM 600 Scanning Electron Microscope (SEM) to understand the role played by various defects in the fracture process.

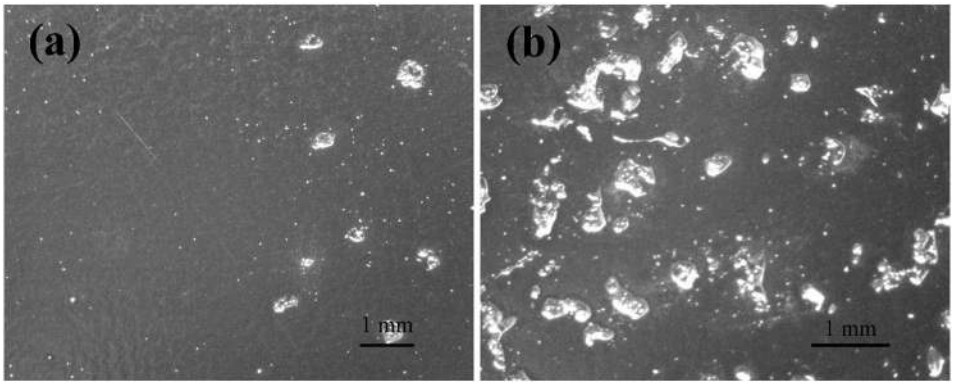

Fig. 2. Macrographs of EBM samples in as-polished condition: (a) EBM-MP2, (b) EBM-MP3.

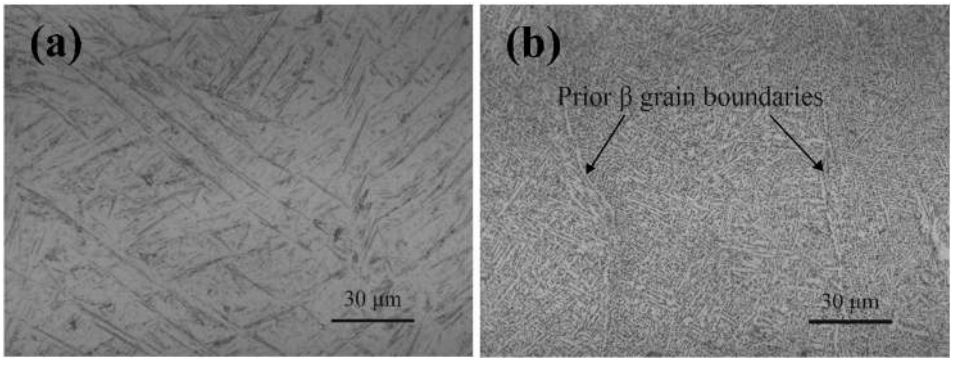

Fig. 3. Optical microstructures of SLM (a) and EBM (b) samples produced using optimum process parameters. Note the presence of α phase (grain boundary α) on prior β grain boundaries in (b).

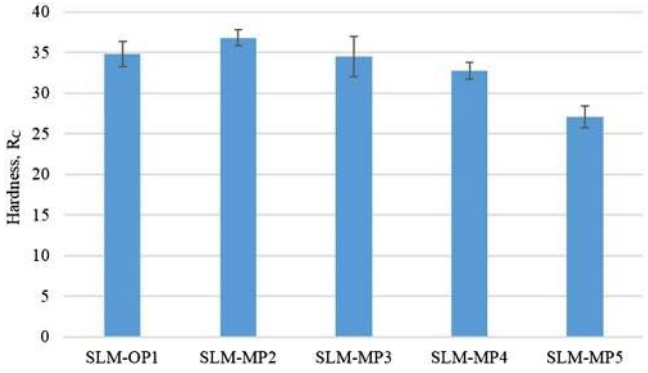

Fig. 4. Hardness of SLM samples.

3. Results and discussion

3.1. Microstructure

SLM samples produced using the optimum process parameters did not show any major defects, except for some sparse pores. Samples produced using lower or higher energy densities contained defects in different amounts, as can be seen in Fig. 1. When the energy density is increased by one level from the optimum, the samples developed small pores (less than 50 μm in size) (Fig. 1a). The pores became larger (up to ~70 μm) with further increase in the energy density (parameter set SLM-MP3) (Fig. 1b). Similarly, when the energy density was reduced by one level, the samples developed some pores (Fig. 1c), which are slightly more irregular and larger in size (up to 110 μm) than those found in the samples produced by increasing the energy density by one level above the optimum. With further decrease in the energy density (parameter set SLM-MP5), the pores became larger in size and more in number (Fig. 1d). The defects in these samples were also more irregular and larger (up to 250 μm in size).

The amount of porosity in all the SLM samples was estimated based on bulk density measurements using the Archimedes method. The results are given in Table 3. The type and nature of defects in SLM parts can be expected to vary depending on the process parameters. At very low energy density levels, pores or voids develop due to incomplete powder melting or improper fusion between successive tracks or layers. In contrast, when the energy density is excessive, the melt pool deepens and pores/voids develop due to entrapped gases or improper closure of the keyhole. Defects of the former type contain unmelted powder in them and samples containing such defects fare better in density measurements than in microscopy. This explains why microscopy revealed relatively more defects in the samples produced using lower-than-optimum energy densities (SLM-MP4 and SLM-MP5) than those produced using higher-than-optimum energy densities (SLM-MP2 and SLM-MP3) at similar amounts of porosity estimated from the Archimedes method. The authors believe that the accuracy of Archimedes density measurements depends on the nature and type of defects in the parts. Archimedes density measurements tend to be more accurate and compare well with microscopic observations when most of the defects do not have entrapped powder in them (i.e., defects resulting from the use of excessive energy input) than when most of the defects are filled with unmelted powder (i.e., defects resulting from the use of insufficient energy input). Further, the results from Archimedes method can considerably vary depending on the surface roughness of the samples. Another issue is sensitivity. The SLM and EBM samples built using optimum parameters in this study indeed contained some sparse porosity defects as revealed in microscopy, but showed an Archimedes density equal to the nominal density of alloy Ti–6Al–4 V. While such samples can be regarded as "fully dense" for most practical purposes, they are not "flawless" and do contain some defects, which can be detrimental to their mechanical properties. Therefore, Archimedes density measurements cannot be entirely relied upon in assessing the quality of SLM or EBM parts. Overall, there is a need for developing methods for determining the density of SLM and EBM parts with greater precision and accuracy.

Density measurements on EBM-MP2 and EBM-MP3 samples indicated that they contained defects amounting to 1 and 5 vol.%, respectively. However, observations revealed that these samples were far more inferior in quality, containing large macroscopic voids filled with unmelted powder particles (because of insufficient energy input) (Fig. 2). Compared to the SLM samples, the size and number of defects in the EBM samples are clearly higher although their bulk densities as determined from the Archimedes method are comparable (because of the presence of more unmelted powder in EBM samples).

Representative optical micrographs of the SLM and EBM samples are shown in Fig. 3. All the SLM samples showed very similar microstructures consisting of primarily acicular martensitic alpha (α′), as can be seen in Fig. 3a. In contrast, the EBM samples showed fine lamellar α-β microstructure (Fig. 3b), suggesting diffusional transformation of the β phase during cooling from high temperature. This is understandable as the cooling rates in EBM are much lower than those in SLM (the powder bed in EBM is maintained at an elevated temperature, around 675 °C, throughout part fabrication). These microstructures are typical of SLM and EBM builds in Ti–6Al–4 V and have been discussed by many earlier investigators [12,39,40]. Overall, the results show that microstructure evolution during SLM and EBM processing of Ti–6Al–4 V

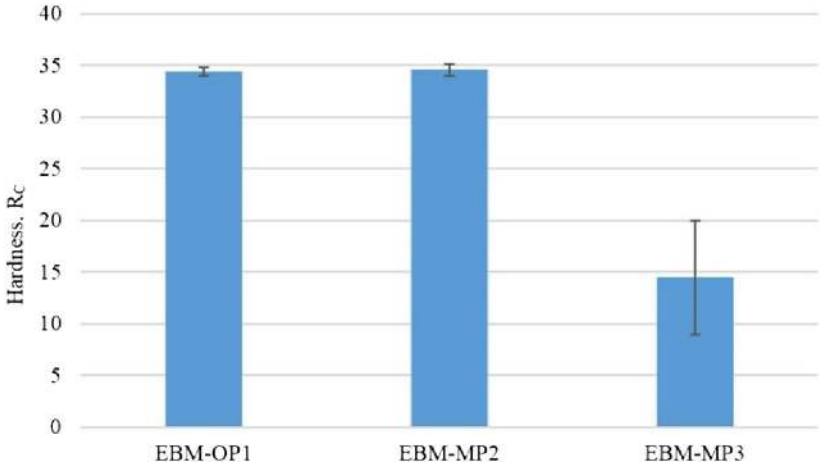

Fig. 5. Hardness of EBM samples.

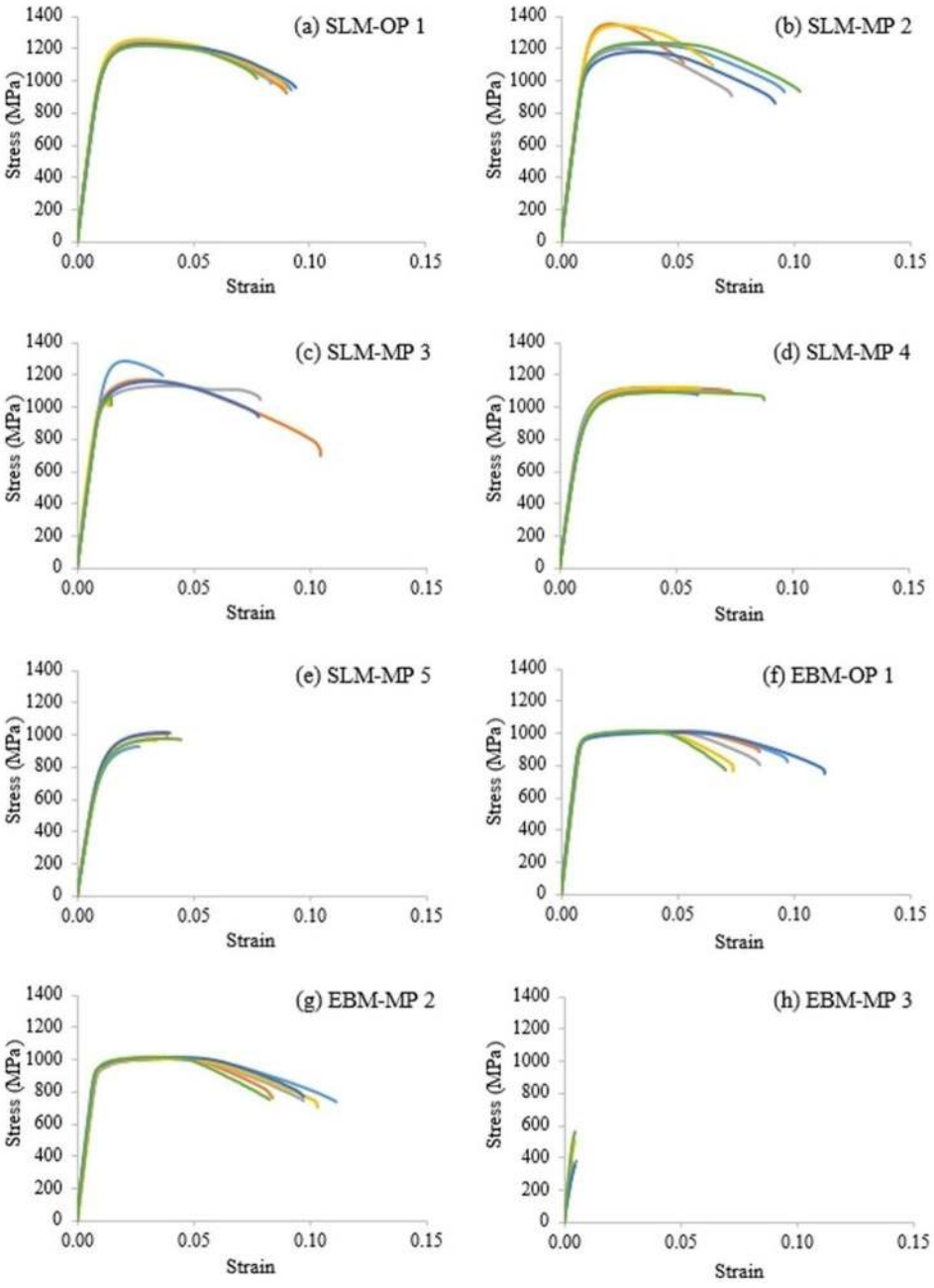

Fig. 6. Stress–strain plots of SLM- and EBM-produced Ti–6Al–4 V specimens.

Table 4
Tensile properties of SLM and EBM samples.

Parameter set	0.2% proof stress (MPa)	UTS (MPa)	Elongation (%)	Young's modulus (GPa)
SLM				
SLM-OP 1	1098 (15)	1237 (13)	8.8 (0.6)	109 (2.1)
SLM-MP 2	1150 (91)	1257 (74)	8.0 (2.0)	111 (1.4)
SLM-MP 3	1066 (91)	1148 (80)	5.4 (3.8)	109 (3.7)
SLM-MP 4	932 (16)	1112 (13)	6.6 (1.4)	95 (3.0)
SLM-MP 5	813 (23)	978 (32)	3.7 (0.6)	84 (3.0)
EBM				
EBM-OP 1	962 (4.0)	1012 (3.0)	8.8 (1.6)	121 (3.0)
EBM-MP 2	947 (11)	1011 (4.0)	9.0 (1.1)	120 (9.0)
EBM-MP 3	–	423 (88)	0.4 (0.1)	92 (20)

primarily depends on the cooling rate and defects such as pores and voids have little effect on the intragranular microstructure (phase constitution and morphology).

3.2. Hardness

The results of Rockwell hardness testing on SLM and EBM samples are shown in Figs. 4 and 5, respectively. SLM-OP1, SLM-MP2, and SLMP3 samples showed a similar hardness. Even SLM-MP4 samples showed only a slight drop in hardness, but SLM-MP5 samples showed significantly lower hardness. Among the three EBM samples, EBM-OP1 and EBM-MP2 samples showed more or less the same hardness, but EBM-MP2 samples showed drastically lower hardness. It may be also noticed that the hardness of SLM and EBM samples produced under optimum conditions is similar, notwithstanding the differences in their microstructure. These results show that small pores do not affect the hardness of Ti–

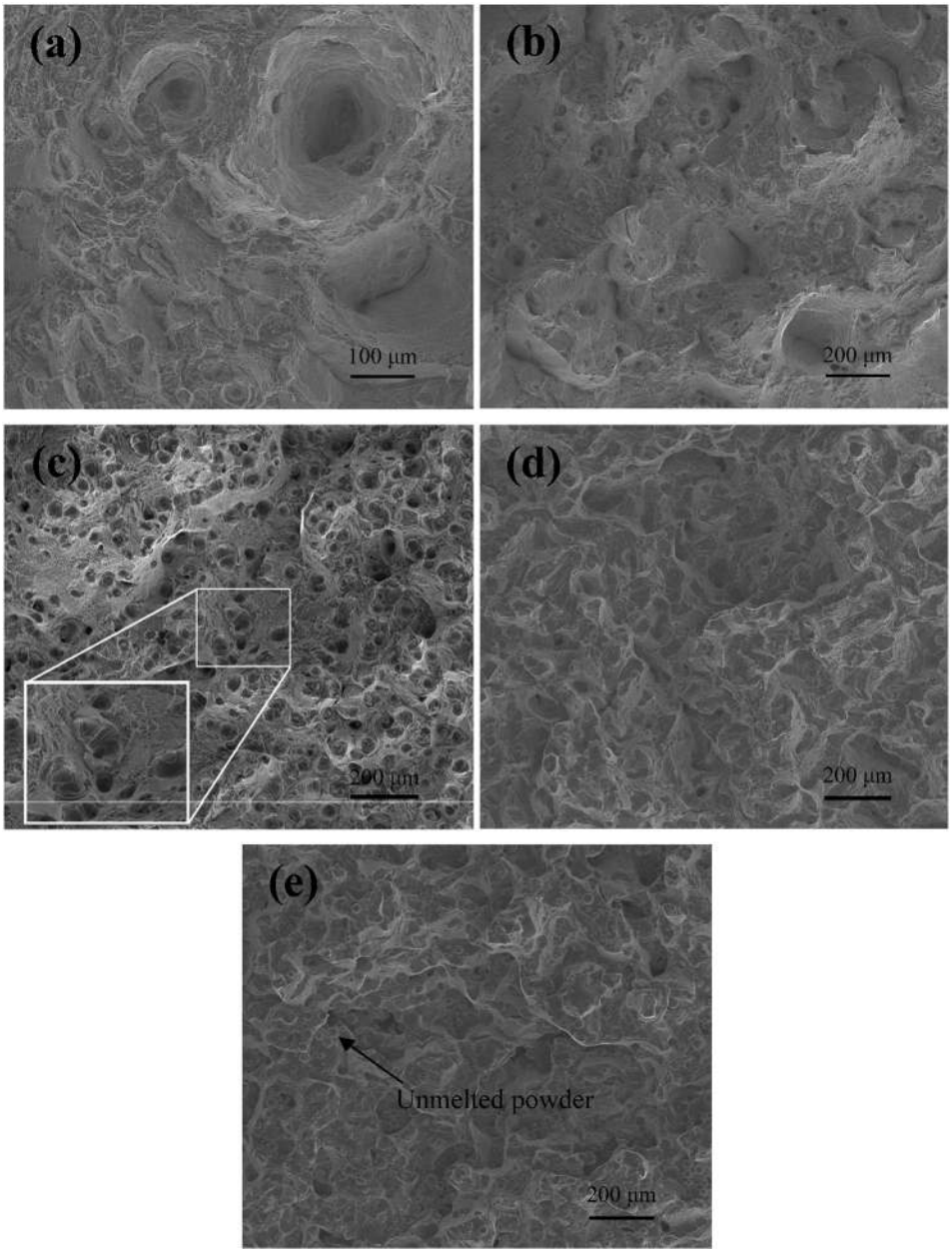

Fig. 7. Tensile fracture surfaces of SLM samples: (a) SLM-OP, (b) SLM-MP2, (c) SLM-MP3, (d) SLM-MP4, (e) SLM-MP5.

6Al–4 V parts produced by SLM and EBM. However, when the energy input is very low, the parts develop large voids due to incomplete powder melting, which impair their hardness significantly.

3.3. Tensile properties

Fig. 6 shows the stress–strain plots of SLM and EBM specimens. For each process parameter set, multiple specimens were tested. The average yield strength, ultimate tensile strength (UTS), Young's modulus and % elongation values are summarized in Table 4. The tensile properties obtained on SLM and EBM samples built under optimum conditions (SLM-OP1 and EBM-OP1) compare well with available published test data [12,41]. As reported by earlier investigators [40], the SLM samples showed higher yield and tensile strengths than the EBM samples because of their predominantly martensitic α microstructure. The SLM samples showed decent tensile ductility (as good as EBM samples), suggesting that their microstructure is not fully martensitic.

SLM samples produced using parameter set SLM-MP2 showed similar tensile properties to those produced under optimum conditions, while parameter set SLM-MP3 resulted in some drop in UTS and % elongation. Samples produced using parameter set SLM-MP4 showed further degradation, while those produced using parameter set SLM-MP5 showed the lowest strength and ductility. Overall, the defects generated due to insufficient energy input appear to be more detrimental to part mechanical properties than those generated due to excessive energy input. In other words, the results show that the SLM process is more tolerant to a little excess energy input than insufficient energy input. With regard to EBM, parameter set EBM-MP2 did not result in any significant reduction in tensile properties, but the samples built using parameter set EBM-MP3 performed very poorly in tensile tests.

Representative tensile fracture surfaces of various SLM and EBM samples are shown in Figs. 7 and 8, respectively. Both SLM and EBM samples produced under optimum conditions showed ductile dimpled rupture features (Figs. 7a and 8a). The fracture surfaces of SLM-MP2 and EBM-MP2 samples also appeared very similar to those of SLM-

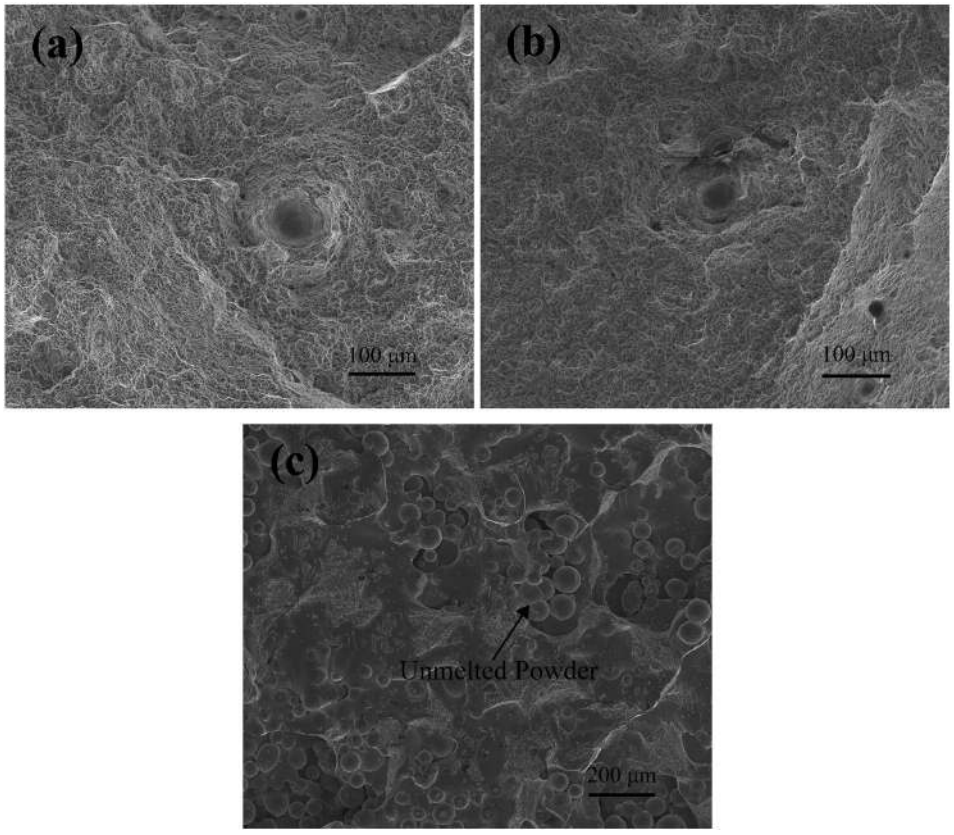

Fig. 8. Tensile fracture surfaces of EBM samples: (a) EBM-OP1, (b) EBM-MP2, (c) EBM-MP3.

OP1 and EBM-OP1 samples, respectively, but contained a few discernible pores and voids (compare Fig. 7a and b; Fig. 8a and b). The defects in SLM-MP3 samples could be readily seen on their fracture surfaces, as shown in Fig. 7c. SLM-MP4 samples showed ductile dimpled rupture features with some regions of brittle fracture corresponding to lack-of-fusion defects (Fig. 7d). Fracture surfaces of SLM-MP5 and EBM-MP3 samples revealed numerous unmelted powder particles, as can be seen from Figs. 7e and 8c, respectively.

3.4. Fatigue properties

The results of fatigue testing on SLM and EBM samples are shown in Figs. 9 and 10, respectively. All the samples, including those produced under optimum conditions, showed considerable scatter in fatigue life. The fatigue limit of SLM samples produced under optimum conditions in this study was found to be considerably lower (350 MPa) than that (550 MPa) reported by Rafi et al. [40] for Ti–6Al–4 V SLM samples produced using EOS supplied Ti–6Al–4 V powder and EOS recommended process parameters. The Ti–6Al–4 V powder used in the current study has a different particle size distribution from the EOS Ti–6Al–4 V powder. Further, the process parameters used in the current study were also considerably different from those recommended by EOS. While detailed one-to-one comparisons are needed to ascertain the key differences, in terms of overall quality, the samples produced in the current study appear to be inferior to those in Ref. [40].

Among the SLM samples, SLM-MP2 samples showed comparable fatigue performance to SLM-OP1 samples. However, SLM-MP3 samples showed noticeable drop in fatigue lives and fatigue limit (300 MPa) due to the presence of pores in larger size and number. The samples built using lower-than-optimum energy densities (SLM-MP4 and

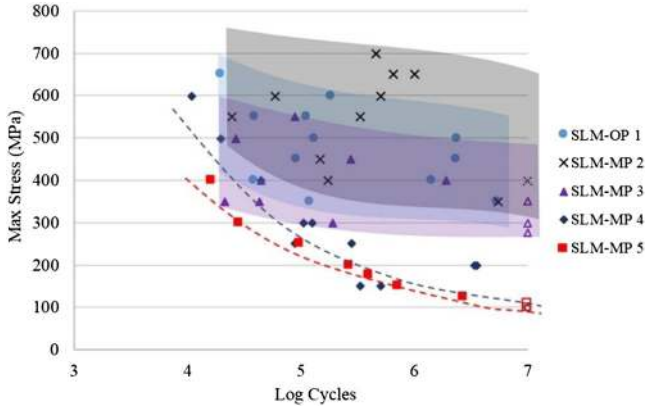

Fig. 9. Fatigue lives of SLM-produced Ti–6Al–4 V specimens.

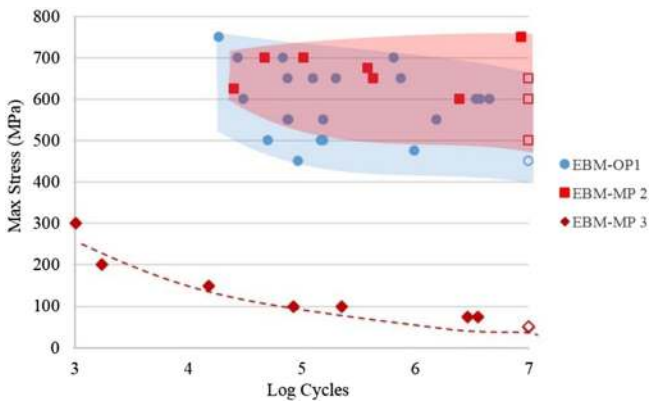

Fig. 10. Fatigue lives of EBM-produced Ti–6Al–4 V specimens.

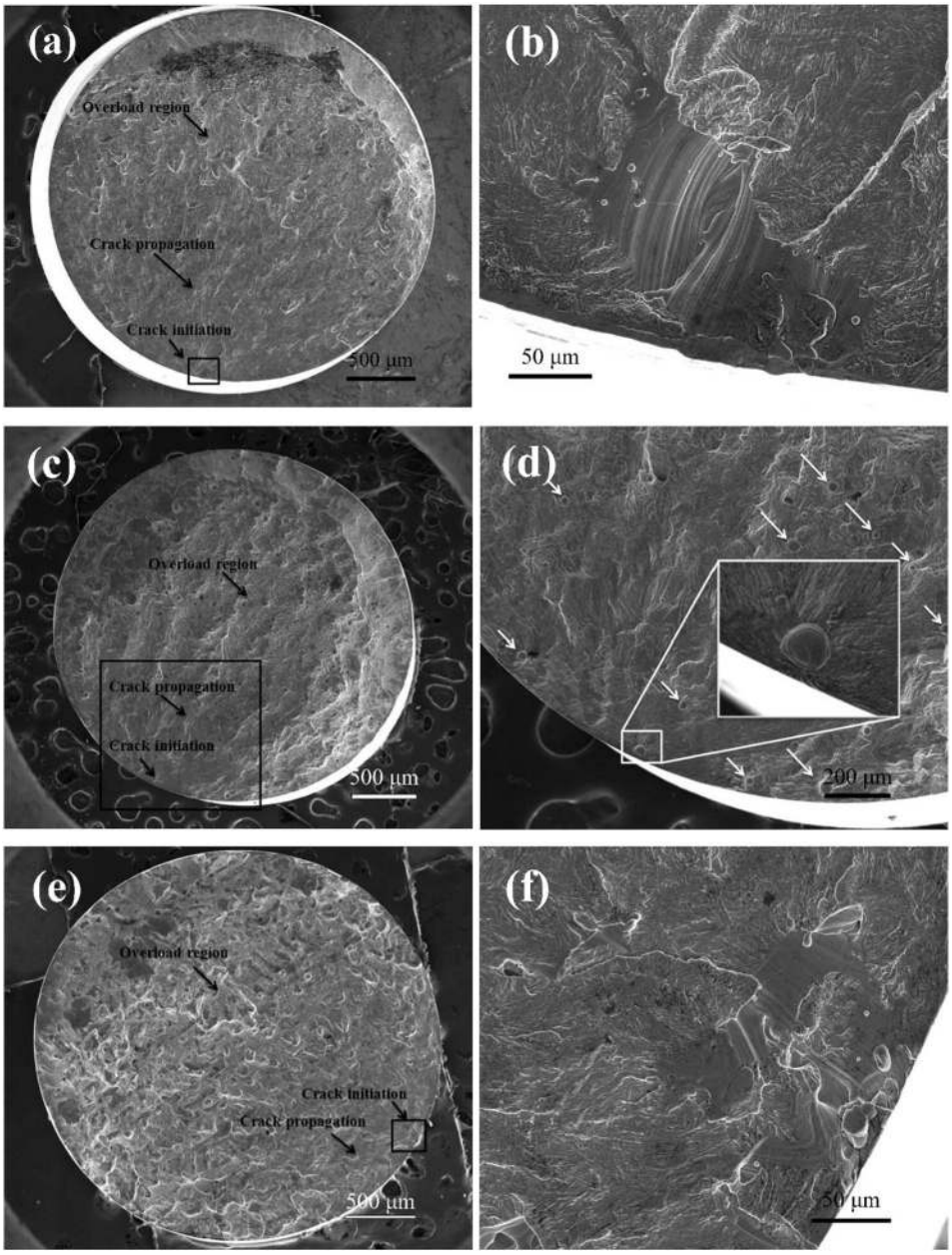

Fig. 11. Fracture surfaces of SLM fatigue specimens: (a) and (b) SLM-OP1, (c) and (d) SLM-MP2, (e) and (f) SLM-MP4. The images on the left are taken at low magnification and show the entire specimen cross-section. The rectangular boxes show the regions of crack initiation. White arrows show the defects. The images on the right show the fracture features at a higher magnification close to the crack origin.

SLM-MP5) showed a fatigue limit of around 100 MPa confirming that defects due to lack-of-fusion and incomplete powder melting are seriously detrimental to the fatigue performance. It should be noted that these samples show a very definite trend of increasing fatigue life with decreasing stress amplitude, unlike the other three sets of SLM samples. This suggests that lack-of-fusion defects in SLM-MP4 and SLM-MP5 samples are so seriously detrimental to fatigue performance that even the statistical nature of metal fatigue is defeated. In the case of EBM, EMB-OP1 and EBM-MP2 samples showed comparable fatigue lives, but the fatigue performance of EBM-MP3 samples is very poor with a fatigue limit of just 50 MPa. As in the case of SLM-MP4 and SLM-MP5 samples, EBM-MP3 samples showed a very regular trend of increasing fatigue life with decreasing stress amplitude, unlike EBM-OP1 and EBM-MP2 samples.

Representative fractographs of SLM and EBM fatigue fractured specimens are shown in Figs. 11 and 12, respectively. In all the specimens, including those built using optimum parameters (Fig. 11a and b, Fig. 12a and b), cracks were found to initiate at a defect near the surface or subsurface. The fracture surfaces of SLM-MP2 specimens (Fig. 11c and d) revealed smaller and more regularly shaped defects compared to SLM-MP4 specimens (Fig. 11e and f). Spherical powder particles evidencing incomplete melting were also seen on the fracture surfaces of SLM-MP4 samples. These features can be seen more clearly in EBM-MP3 samples (Fig. 12c and d). Finally, the spherical defects evident on tensile (Fig. 7b) and fatigue (Fig. 11d) fracture surfaces of SLM-MP2 samples have a “stair” feature on their internal surface that may merit further investigation. The spherical defects could result from gas bubbles entrapped or generated when a high laser energy is applied to the melt pool, or from the pits generated by the recoater blade when removing welded particles [35,42,43]. But according to the morphological features and distribution, gas bubbles account for most of these defects in SLM-MP2 specimens.

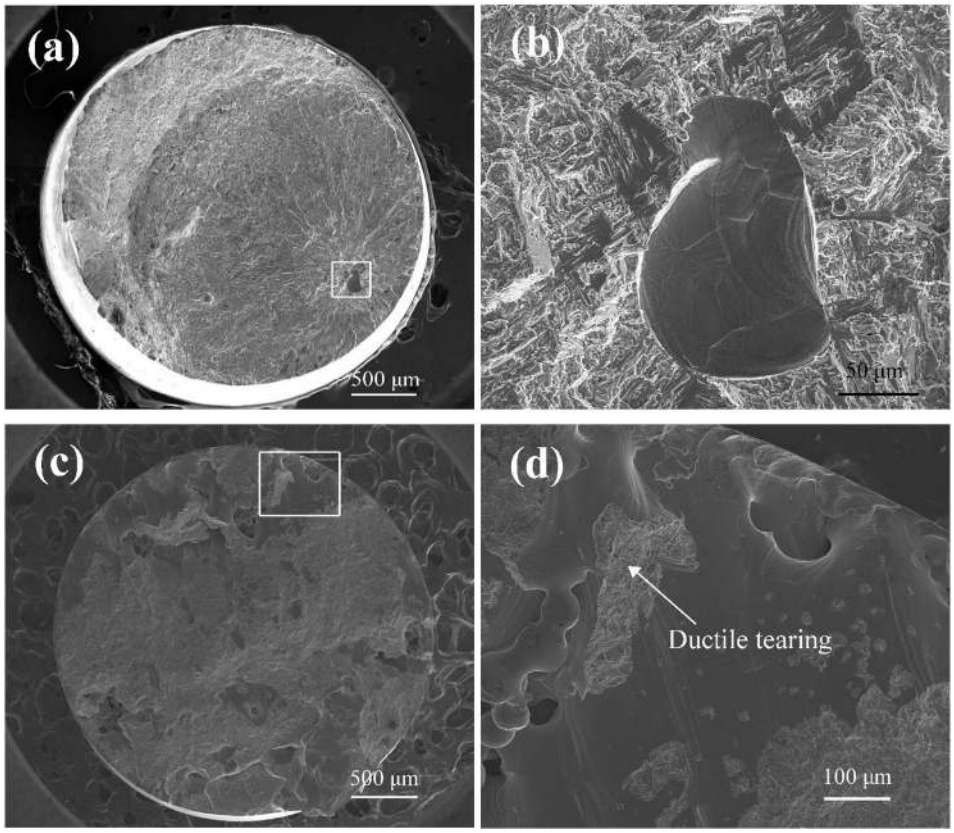

Fig. 12. Fracture surfaces of EBM specimens: (a) and (b) EBM-OP1, (c) and (d) EBM-MP3. The images on the left are taken at low magnification and show the entire specimen cross-section. The rectangular boxes show the regions of crack initiation. The images on the right show the fracture features at a higher magnification close to the crack origin.

4. Conclusions

In this study, SLM and EBM processes were used to produce Ti–6Al–4 V samples with different types and amounts of defects. The samples were subjected to hardness, tensile, and fatigue tests. Based on the findings of this study, the following conclusions can be drawn:

- Defect generation does not influence microstructure evolution in Ti–6Al–4 V during SLM and EBM. The microstructure is mainly governed by the cooling rate.
- Ti–6Al–4 V samples built using SLM show higher yield and tensile strengths than those produced using EBM because of their predominantly martensitic α microstructure. However, SLM and EBM samples show comparable tensile ductility, fatigue strength, and hardness.
- Density measurements using the Archimedes method are not satisfactory for assessing the quality of SLM and EBM samples, particularly when the samples are built using insufficient energy input. Samples may contain a significant amount of unmelted powder inside the defects, which contributes to density, but not to strength.
- In SLM samples, small pores or voids caused by the use of higher-than-optimum energy input are harmless when present in amounts up to 1 vol.%. However, tensile, fatigue, and hardness properties are considerably affected when these defects occur at the level of 5 vol.%.
- In SLM, defects caused by insufficient energy input have a strong bearing on the mechanical properties even when present in amounts as low as 1 vol.%. When such defects occur in higher amounts (to the level of 5 vol.%), the part mechanical properties tend to be very poor and unacceptable.
- In SLM, defects caused by excessive energy input are less detrimental to part mechanical properties than those caused by insufficient energy input.
- In EBM, any significant deviation from optimum process parameters results in relatively large defects and poor mechanical properties.

Acknowledgments

The authors gratefully acknowledge the support of the Office of Naval Research, awards N00014-09-1-0147 and N00014-10-1-0800, Technical Monitor: Dr. Ignacio Perez. The authors also express their gratitude to the staff of Rapid Prototyping Center at the University of Louisville for their assistance.

References

[1] I. Gibson, D.W. Rosen, B. Stucker, Additive manufacturing technologies: rapid prototyping to direct digital manufacturing, Springer, New York, 2009.
[2] T.H.C. Childs, C. Hauser, M. Badrossamay, Selective laser sintering (melting) of stainless and tool steel powders: experiments and modelling, Proc. Inst. Mech. Eng. B J. Eng. Manuf. 219 (2005) 339–357.
[3] G. Casalino, S.L. Campanelli, N. Contuzzi, A.D. Ludovico, Experimental investigation and statistical optimisation of the selective laser melting process of a maraging steel, Opt. Laser Technol. 65 (2015) 151–158.
[4] B. Vandenbroucke, J.P. Kruth, Selective laser melting of biocompatible metals for rapid manufacturing of medical parts, Rapid Prototyp. J. 13 (2007) 196–203.
[5] S. Price, B. Cheng, J. Lydon, K. Cooper, K. Chou, On process temperature in powder-bed electron beam additive manufacturing: process parameter effects, J. Manuf. Sci. Eng. 136 (2014) (061019-1-10).
[6] S. Sun, Y. Koizumi, S. Kurosu, Y. Li, H. Matsumoto, A. Chiba, Build direction dependence of microstructure and high-temperature tensile property of Co–Cr–Mo alloy fabricated by electron beam melting, Acta Mater. 64 (2014) 154–168.
[7] L. Thijs, F. Verhaeghe, T. Craeghs, J.V. Humbeeck, J.P. Kruth, A study of the microstructural evolution during selective laser melting of Ti–6Al–4 V, Acta Mater. 58 (2010) 3303–3312.
[8] N. Tolochko, S. Mozzharov, I. Yadroitsev, Balling processes during selective laser treatment of powders, Rapid Prototyp. J. 10 (2004) 78–87.
[9] R. Li, J. Liu, Y. Shi, M. Du, X. Zhan, 316 L stainless steel with gradient porosity fabricated by selective laser melting, J. Mater. Eng. Perform. 19 (2010) 666–671.

[10] S. Biamino, A. Penna, U. Ackelid, S. Sabbadini, O. Tassa, P. Fino, et al., Electron beam melting of Ti–48Al–2Cr–2Nb alloy: microstructure and mechanical properties investigation, Intermet 19 (2011) 776–781.
[11] L. Facchini, E. Magalini, P. Robotti, A. Molinari, S. Höges, K. Wissenbach, Ductility of a Ti–6Al–4 V alloy produced by selective laser melting of prealloyed powders, Rapid Prototyp. J. 16 (2010) 450–459.
[12] L. Facchini, E. Magalini, P. Robotti, A. Molinari, Microstructure and mechanical properties of Ti–6Al–4 V produced by electron beam melting of pre-alloyed powders, Rapid Prototyp. J. 15 (2009) 171–178.
[13] E. Wycisk, C. Emmelmann, S. Siddique, F. Walther, High cycle fatigue (HCF) performance of Ti–6Al–4 V alloy processed by selective laser melting, Adv. Mater. Res. 816–817 (2013) 134–139.
[14] G.V. Joshi, Y. Duan, J. Neidigh, M. Koike, G. Chahine, R. Kovacevic, et al., Fatigue testing of electron beam-melted Ti–6Al–4 V ELI alloy for dental implants, J. Biomed. Mater. Res. B Appl. Biomater. 101B (2013) 124–130.
[15] T. Sercombe, N. Jones, R. Day, A. Kop, Heat treatment of Ti–6Al–7Nb components produced by selective laser melting, Rapid Prototyp. J. 14 (2008) 300–304.
[16] Q. Liu, J. Elambasseril, S. Sun, M. Leary, M. Brandt, P.K. Sharp, The effect of manufacturing defects on the fatigue behaviour of Ti–6Al–4 V specimens fabricated using selective laser melting, Adv. Mater. Res. 891–892 (2014) 1519–1524.
[17] E. Santos, F. Abe, Y. Kitamura, K. Osakada, M. Shiomi, Mechanical properties of pure titanium models processed by selective laser melting, 13rd Annual International Solid Freeform Fabrication Symposium, Austin TX 2002, pp. 180–186.
[18] H. Gong, K. Rafi, T. Starr, B. Stucker, Effect of defects on fatigue tests of as-built Ti–6Al–4 V parts fabricated by selective laser melting, 23rd Annual International Solid Freeform Fabrication Symposium, Austin TX 2012, pp. 499–506.
[19] P. Edwards, M. Ramulu, P. Edwards, M. Ramulu, Fatigue performance evaluation of selective laser melted Ti–6Al–4 V, Mater. Sci. Eng. A 598 (2014) 327–337.
[20] E. Wycisk, A. Solbach, S. Siddique, D. Herzog, F. Walther, C. Emmelmann, Effects of defects in laser additive manufactured Ti–6Al–4 V on fatigue properties, Phys. Procedia 56 (2014) 371–378.
[21] M. Simonelli, Y.Y. Tse, C. Tuck, Fracture mechanisms in high-cycle fatigue of selective laser melted Ti–6Al–4 V, Key Eng. Mater. 627 (2015) 125–128.
[22] S. Leuders, M. Thöne, A. Riemer, T. Niendorf, T. Tröster, H.A. Richard, et al., On the mechanical behaviour of titanium alloy TiAl6V4 manufactured by selective laser melting: fatigue resistance and crack growth performance, Int. J. Fatigue 48 (2013) 300–307.
[23] S.J. Li, L.E. Murr, Z.B. Zhang, X.Y. Cheng, Y.L. Hao, R. Yang, et al., Compression fatigue behavior of Ti–6Al–4 V mesh arrays fabricated by electron beam melting, Acta Mater. 60 (2012) 793–802.
[24] F. Brenne, T. Niendorf, H.J. Maier, Additively manufactured cellular structures: impact of microstructure and local strains on the monotonic and cyclic behavior under uniaxial and bending load, J. Mater. Process. Technol. 213 (2013) 1558–1564.
[25] J. Sun, Y. Yang, D. Wang, Mechanical properties of a Ti6Al4V porous structure produced by selective laser melting, Mater. Des. 49 (2013) 545–552.
[26] S. Amin Yavari, S.M. Ahmadi, R. Wauthle, B. Pouran, J. Schrooten, H. Weinans, et al., Relationship between unit cell type and porosity and the fatigue behavior of selective laser melted meta-biomaterials, J. Mech. Behav. Biomed. Mater. 43 (2015) 91–100.
[27] P. Heinl, C. Körner, R.F. Singer, Selective electron beam melting of cellular titanium: mechanical properties, Adv. Eng. Mater. 10 (2008) 882–888.
[28] L.E. Murr, S.M. Gaytan, F. Medina, E. Martinez, J.L. Martinez, D.H. Hernandez, et al., Characterization of Ti–6Al–4 V open cellular foams fabricated by additive manufacturing using electron beam melting, Mater. Sci. Eng. A 527 (2010) 1861–1868.
[29] L.E. Murr, K.N. Amato, S.J. Li, Y.X. Tian, X.Y. Cheng, S.M. Gaytan, et al., Microstructure and mechanical properties of open-cellular biomaterials prototypes for total knee replacement implants fabricated by electron beam melting, J. Mech. Behav. Biomed. Mater. 4 (2011) 1396–1411.
[30] J. Schwerdtfeger, P. Heinl, R.F. Singer, C. Körner, Auxetic cellular structures through selective electron-beam melting, Phys. Status Solidi B 247 (2010) 269–272.
[31] J. Schwerdtfeger, F. Schury, M. Stingl, F. Wein, R.F. Singer, C. Körner, Mechanical characterisation of a periodic auxetic structure produced by SEBM, Phys. Status Solidi B 249 (2012) 1347–1352.
[32] S.J. Li, Q.S. Xu, Z. Wang, W.T. Hou, Y.L. Hao, R. Yang, et al., Influence of cell shape on mechanical properties of Ti–6Al–4 V meshes fabricated by electron beam melting method, Acta Biomater. 10 (2014) 4537–4547.
[33] L. Yang, O. Harrysson, H. West, D. Cormier, Compressive properties of Ti–6Al–4 V auxetic mesh structures made by electron beam melting, Acta Mater. 60 (2012) 3370–3379.
[34] B. Song, S. Dong, B. Zhang, H. Liao, C. Coddet, Effects of processing parameters on microstructure and mechanical property of selective laser melted Ti6Al4V, Mater. Des. 35 (2012) 120–125.
[35] H. Gong, K. Rafi, H. Gu, T. Starr, B. Stucker, Analysis of defect generation in Ti–6Al–4 V parts made using powder bed fusion additive manufacturing processes, Addit. Manuf. 1 (2014) 87–98.
[36] H. Gong, K. Rafi, N.V. Karthik, T. Starr, B. Stucker, Defect morphology in Ti–6Al–4 V parts fabricated by selective laser melting and electron beam melting, 24th Annual International Solid Freeform Fabrication Symposium, Austin TX 2013, pp. 440–453.
[37] S. Zhang, Q. Wei, L. Cheng, S. Li, Y. Shi, Effects of scan line spacing on pore characteristics and mechanical properties of porous Ti6Al4V implants fabricated by selective laser melting, Mater. Des. 63 (2014) 185–193.
[38] N. Hrabe, T. Quinn, Effects of processing on microstructure and mechanical properties of a titanium alloy (Ti–6Al–4 V) fabricated using electron beam melting (EBM), Part 2: energy input, orientation, and location, Mater. Sci. Eng. A 573 (2013) 271–277.
[39] M. Simonelli, Y.Y. Tse, C. Tuck, Microstructure of Ti–6Al–4 V produced by selective laser melting, J Phys Conf Ser, 371 2012, p. 012084.
[40] K. Rafi, N.V. Karthik, H. Gong, T. Starr, B. Stucker, Microstructures and mechanical properties of Ti–6Al–4 V parts made by selective laser melting and electron beam melting, J. Mater. Eng. Perform. 22 (2013) 3872–3883.
[41] K. Rafi, T. Starr, B. Stucker, A comparison of the tensile, fatigue, and fracture behavior of Ti–6Al–4 V and 15–5 PH stainless steel parts made by selective laser melting, Int. J. Adv. Manuf. Technol. 69 (2013) 1299–1309.
[42] L. Li, Repair of directionally solidified superalloy GTD-111 by laser-engineered net shaping, J. Mater. Sci. 41 (2006) 7886–7893.
[43] W.E. King, H.D. Barth, V.M. Castillo, G.F. Gallegos, J.W. Gibbs, D.E. Hahn, et al., Observation of keyhole-mode laser melting in laser powder-bed fusion additive manufacturing, J. Mater. Process. Technol. 214 (2014) 2915–2925.